

A mobile antineutrino detector with plastic scintillators

Y. Kuroda^{a,1}, S. Oguri^{a,1}, Y. Kato^a, R. Nakata^a, Y. Inoue^b, C. Ito^c, M. Minowa^a

^a*Department of Physics, School of Science, University of Tokyo, 7-3-1, Hongo, Bunkyo-ku, Tokyo 133-0033, Japan*

^b*International Center for Elementary Particle Physics, University of Tokyo, 7-3-1, Hongo, Bunkyo-ku, Tokyo 133-0033, Japan*

^c*Oarai Research and Development Center, Japan Atomic Energy Agency, 4002, Naritacho, Oarai, Ibaraki 311-1393, Japan*

Abstract

We propose a new type segmented antineutrino detector made of plastic scintillators for the nuclear safeguard application. A small prototype was built and tested to measure background events. A satisfactory unmanned field operation of the detector system was demonstrated. Besides, a detailed Monte Carlo simulation code was developed to estimate the antineutrino detection efficiency of the detector.

Keywords: reactor, safeguards, neutrino, antineutrino,

1. Introduction

Nuclear power plants are the most intense man-controlled sources of neutrinos. With an average energy of about 200 MeV released per fission and about 6 neutrinos produced along the β -decay chain of the fission products, a total flux of $2 \times 10^{20} \nu/s$ is emitted by a 1-GWt power plant. Since un-

Email address: k@icepp.s.u-tokyo.ac.jp (Y. Kuroda)

¹Research Fellow of the Japan Society for the Promotion of Science

stable fission products are neutron-rich nuclei, all β -decays are of β^- type and the neutrino flux is actually of pure electron antineutrinos ($\bar{\nu}_e$). A prediction of its production rate and spectrum associated with the fission of ^{235}U , ^{238}U , ^{239}Pu and ^{241}Pu exists and was recently revisited[1][2][3].

The International Atomic Energy Agency uses an ensemble of procedures and technologies, collectively referred to as the Safeguards Regime, to detect diversion of fissile materials from civil nuclear fuel cycle facilities into weapons programs. One can ensure by measuring antineutrinos that a reactor was not stopped or started with unusual frequency. Moreover, the rate and energy spectrum measurements enable a non-intrusive, real-time estimate of instantaneous and integrated thermal power and provide the information of the isotopic content of the in-core fuel.

Such a concept of antineutrino detection was first performed by a Russian group at the Rovno Nuclear Power Plant in Ukraine[4]. Recently another experiment has been done at the San Onofre Nuclear Generating Station in the USA using organic-liquid-scintillator detector with cubic meter scale in an underground gallery[5],[6]. They demonstrated a clear correlation between the changes in the reactor antineutrino emission rate and the evolution of the reactor power and fissile inventory[7]. These experiments have shown practical capabilities suitable for near term use in the safeguards context. In addition, a study of neutrino detection with a compact liquid scintillator detector deployed at the ground level was recently carried out at the experimental fast reactor in Japan[8].

To improve the safety characteristics and make deployments and operations easier, use of plastic detectors has some advantages. Current liquid

scintillators are usually based on organic solvents and therefore have some security (toxicity and flammability) issues, chemical compatibility with the container (they are good solvents) and need complicated retaining structures.

Additionally, detector mobility, simple installation and sea-level operation of detectors, rather than underground have great impact for safeguards applications.

Taking above points into account, we propose a simple and mobile antineutrino detector, “PANDA”, which stands for Plastic Anti-Neutrino Detector Array. The detector is made of plastic scintillators. It can be installed on a dry van and placed outside of a reactor building (easily accessible zone).

Although these features have advantages in safeguards applications, there are some drawbacks. Using plastic scintillators leads to some reduction in overall detection efficiency due to their smaller number of protons per volume comparing to typical liquid scintillators used in other neutrino experiments. Furthermore, above-ground detection is a challenge because of the backgrounds induced by cosmic rays. For inverse-beta detectors, the correlated background event rate at sea-level may increase substantially relative to underground detectors.

In this paper, we report on the details of the proposed PANDA detector and also the performance of a small prototype called Lesser PANDA.

2. Detector layout

The PANDA detector consists of modules made of plastic scintillator bars ($10\text{cm} \times 10\text{cm} \times 100\text{cm}$) wrapped with aluminized Mylar films and gadolinium (Gd) coated Mylar films ($4.9\text{ mg of Gd per cm}^2$). Each bar is connected to

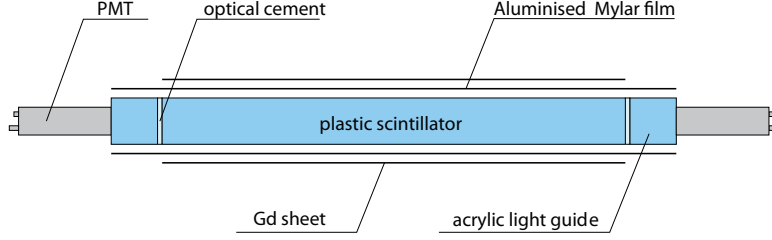
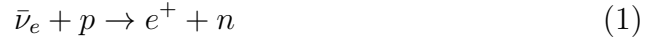


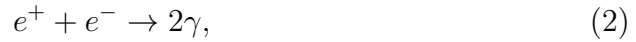
Figure 1: individual module structure

acrylic light guides and photomultipliers on both ends (Fig. 1). The plastic scintillators are Rexon RP-408 and the Gd coated films are manufactured by Ask Sanshin Engineering with their neutron shielding paint. Hamamatsu H6410 (R329-02) PMTs are used for light detection.

Antineutrinos are detected via the inverse beta decay process:



and following reactions:



Here the antineutrino $\bar{\nu}_e$ interacts with the proton p which is present in the plastic scintillator. The neutron n and the positron e^+ are detected by delayed coincidence, providing a dual signature allowing strong rejection of the much more frequent singles backgrounds due to natural radioactivity or cosmogenic neutrons.

The positron deposits energy via Bethe-Bloch ionization as it slows in the scintillator, and upon annihilation with an electron, it emits two gamma

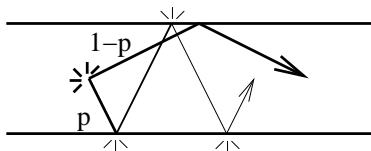


Figure 2: Light propagation model in the plastic scintillator bar

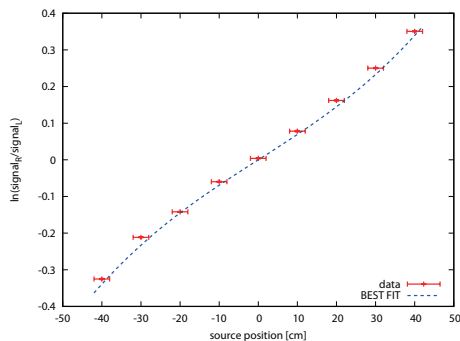


Figure 3: Logarithm of the ratio of PMT charge measured at one end to charge at the other end of the module vs. source position. The dashed curve is a two-parameter (p and l in equation (5)) fit of the ratio predicted by the light attenuation model.

rays which can deposit additional energy of up to 1.022 MeV (reaction (2)). On the other hand the neutron carries away a few keV of energy from the antineutrino interaction and is detected by capture in a Gd on the film with an energy release of ≈ 8 MeV via a gamma ray cascade (reactions (3) and (4)). Reaction (1) has an energy-dependent cross section and a neutrino energy threshold of 1.806 MeV.

The light intensity ratio seen by each PMT pair allows one to estimate the position of the hit along the module. Assuming the fraction p of the light is attenuated in the plastic scintillator exponentially as a function of distance from the point of emission to the PMT and the other $(1 - p)$ propagates

practically without attenuation by repeating total internal reflection at the surface (Fig. 2), the hit position and the light intensity are related through a simple equation:

$$L_{\text{PMT}} = L_{\text{emitted}}((1 - p) + p \exp(-x/l)). \quad (5)$$

In this equation, L_{emitted} and L_{PMT} are the light intensity emitted by the scintillator and reaching the PMT, l is the attenuation length of scintillation light, and x is the distance of the hit position from the PMT. Fig. 3 shows that the above relation (5) fits the data well. Using the position of the hit and the charge outputs from each PMT, one can estimate the energy deposit of the hit. The position and energy resolutions which depend on the deposited energy are about 30 cm and 110 keV for 500 keV hit (10 cm and 300 keV for 4 MeV hit) on the center respectively.

The dependence of the Gd neutron capture efficiency on plastic scintillator granularity and shape were calculated using the simulation toolkit Geant4[9], which offers C++ libraries for simulating the passage of particles. Three types of Gd loading methods were considered: dissolving Gd in plastic scintillators (0.1%wt), placing 25 μm -thick Gd foils ($2.0 \times 10^{-2} \text{g/m}^2$) between scintillator plates (6 cm, 10 cm and 14 cm thick) or wrapping square bars of plastic scintillators (cross-sectional dimensions of 6cm \times 6cm , 10cm \times 10cm and 14cm \times 14cm) with 25 μm -thick Gd foils. In the simulation, the total dimensions in three axes were taken to be infinite.

Ten kiloelectronvolt neutrons were generated at a single point inside of the plastic scintillator, and the probability of capture by Gd and the mean time until the capture were estimated. The results of this study are presented in Table 1. It should be noted here that all neutrons were captured by nuclei

Table 1: Methods of Gd loading and neutron detection efficiency

methods	neutron captured by Gd[%]	mean time until the capture [μ s]
solution 0.1%wt	89.4	28.4
interleaving Gd foils and plastic scintillator sheets of:		
6 cm t	77.0	54.0
10 cm t	62.1	94.9
14 cm t	47.2	138
wrapping Gd foil over plas- tic scintillator bars of:		
6 cm \square	85.7	29.6
10 cm \square	76.0	62.4
14 cm \square	60.2	95.6

of hydrogen or gadolinium.

The simulation result showed that the segmented scintillators interleaved with the gadolinium foils have performance comparable to the gadolinium loaded plastic scintillators. Moreover the technique to produce clear and colorless Gd loaded plastic scintillators is less established. Therefore we did not choose to load gadolinium in scintillators.

Eventually we selected the square bar type module which has an advantage in detecting the positions of energy deposit and therefore energy spectrum of the positrons, which is related directly to the neutrino energy spectrum. The granularity of the modules was determined to be $10\text{ cm} \times 10\text{ cm}$

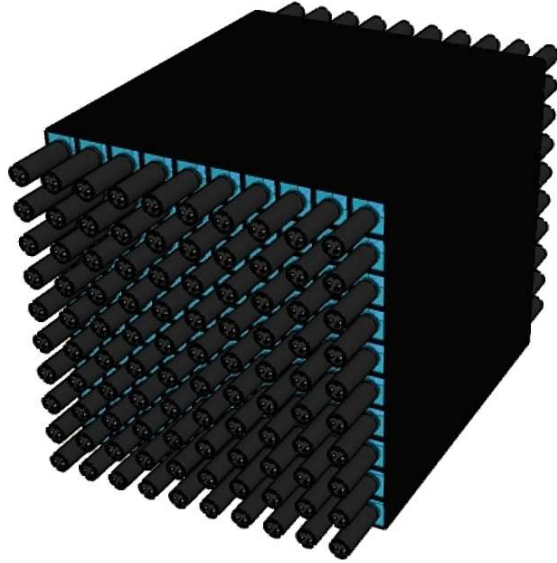


Figure 4: The concept design of the PANDA antineutrino detector. The approximate total target size is 1 m^3 .

taking costs into consideration.

The design of the PANDA detector is shown in Fig. 4. The detector consists of one hundred identical modules described above in this section. As it has fine segmented structure, it becomes possible to use the event topology information to tag anti-neutrino events and to discriminate them from background.

The fine segmentation of the detector also gives the capability to identify and reject passing tracks such as cosmic ray muons. Passing muons are characterized by series of hits distributed along a line in the detector in addition to its relatively large energy deposit. The characteristics helps the PANDA detector to be designed without additional veto counters surrounding the



Figure 5: The prototype detector, Lesser PANDA, consists of 16 modules.

whole detector.

As a first step before building the full-size PANDA detector, a smaller prototype “Lesser PANDA” with 16 modules (Fig. 5) was constructed and was tested by measuring environmental radiation at a commercial reactor. This prototype was used to verify the background rejection ability of its modular configuration with above-ground condition.

3. Electronics and Data Acquisition System

Fig. 6 shows the block diagram of the data acquisition and trigger system for Lesser PANDA. Each PMT signal was divided into two (Fig. 7): 30% of the original charge was sent to CAEN V792 multievent Charge-to-Digital-Converters (QDCs) and the other 70% was passed to Technoland Corporation

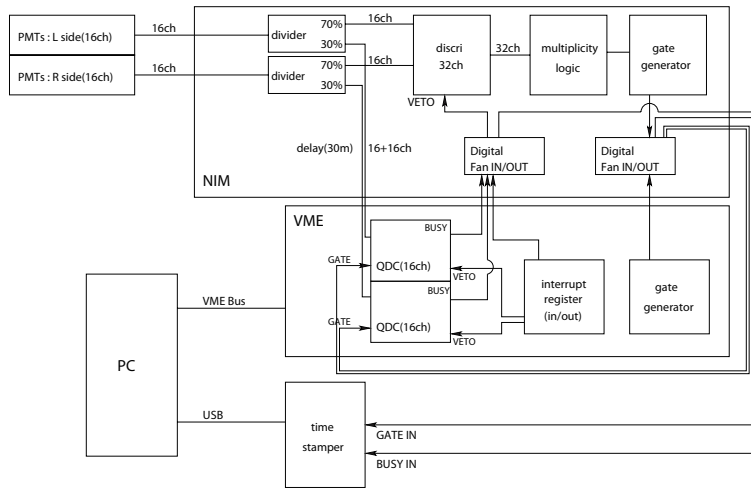


Figure 6: The data acquisition system and trigger logic

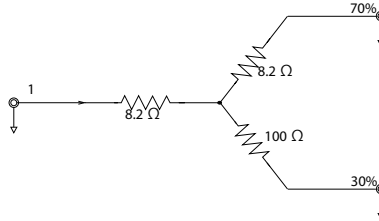


Figure 7: Circuit schematic of signal divider

N-TM 405 leading edge discriminators. Hardware thresholds were set at the lower limit of N-TM 405 which were equivalent to about 150 keV of energy deposit in the plastic scintillators at the far end of the corresponding PMTs.

Gates for the QDCs were produced by the following trigger logic. A hit multiplicity was counted by a REPIC RPN-130 multiplicity logic module and a logic pulse was sent to a gate generator whenever four or more PMTs fired in coincidence with one another giving typical trigger rate of 2.7 kHz. Non-retriggerable logic pulses of 400 ns duration were produced here. The

coincidence width of the multiplicity logic was 50 ns. Although we did not require the triggers to be both pairs of PMTs on two or more scintillator modules, the two-pair condition was applied in the analysis phase. Corresponding to each trigger, the charge outputs of all PMTs were recorded by the QDCs. Meanwhile the trigger timing was recorded by a custom-made time stamper.

We set up periodic pauses of the data acquisition to assure the synchronism of the data from all the QDCs and the time stamper was retained. During the pauses, the data acquisition system counted the number of the collected data and when any mismatches between the QDCs or the time stamper were found, the system discarded all the data after the previous synchronization process.

Due to the conversion times of the QDCs (about $5.7\mu\text{s}$) and synchronization process, the DAQ system had about 3.5% dead time when the trigger rate was 2.7 kHz. The QDCs have 32 event buffer memories and they incur little dead time as long as the read out system can sustain the data rate. The amount of data transferred from QDCs to PC was small enough (≈ 370 kByte/sec) at the assumed trigger rate; therefore the read out dead time was negligible ($< 0.01\%$).

The time stamper was implemented on a Xilinx Spartan-6 FPGA running at 50-MHz clock. The trigger timing information allows to calculate the interval between a pair of events. The time stamper also recorded the timing of the busy signals from QDCs which was used to calculate the dead time of the measurements. These timing information was stored in a cache memory on the FPGA once and sent to a hard disk drive sequentially via USB 2.0

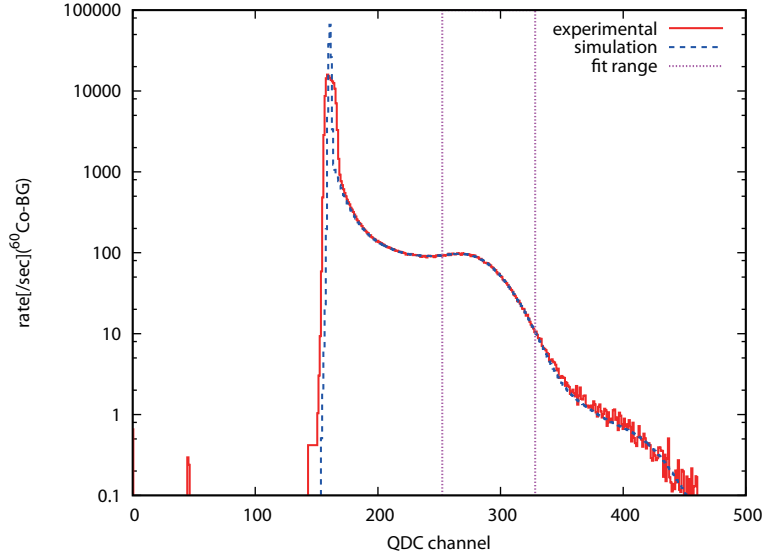


Figure 8: An example of energy spectrum in one module obtained with ^{60}Co calibration source after background subtraction, compared with the Geant4 simulation (dashed line).

(Universal Serial Bus 2.0). The data transfer speed of USB 2.0 is high enough to run without dead time due to the time stamper at trigger rate of 2.7kHz.

Energy calibration of the detector was carried out using a ^{60}Co gamma-ray source temporarily placed at three different positions: the very center of the detector or the centers of both the PMT sides. Calibration constants were evaluated for each module separately.

Multiple Compton scattering of the gamma-rays with energies of 1.17 MeV and 1.33 MeV in the detector or in the surrounding materials and statistical and electronic fluctuation of the output signals produce a broad spectral feature in the measured energy spectrum (Fig. 8). To compare with the measured energy spectrum, we performed a Monte Carlo simulation of gamma-ray transports in the detector using Geant4[9].

The calibration procedure was as follows: we took data with a ^{60}Co source; determined the values of the pedestals; fitted the broad spectral feature by Compton scattering of ^{60}Co gamma-rays of the simulation to the three data at the same time taking into account the light attenuation described in Section 2.

When the detector was in operation, relative gain drift of each module was corrected using gamma-rays arising from natural radioactivity. The background gamma-ray spectrum was taken just after the first calibration as a reference and each data set was compared to it. The gain drift of each PMT was 5.1% on root mean square and corrected every about 6 minutes.

Also the pedestals were monitored. The values of the pedestals were determined from each data set. Since the signals from all modules were digitized simultaneously when any four or more PMTs fired, a large number of recorded events for particular modules had zero energy and were a measurement of the energy pedestal.

The DAQ systems were installed on a dry van with the detector. NTT DoCoMo cell phone network was used for remote monitoring of the detector health status. The remote connection to the system was also used to control the detector system from a distance. The Lesser PANDA system typically operated without physical intervention for two weeks.

4. Detector Simulation

We used Monte Carlo simulations to have insight into the particle transport properties of the PANDA/Lesser PANDA detectors and to estimate the $\bar{\nu}_e$ detection efficiencies of our detectors taking advantage of the fine segmen-

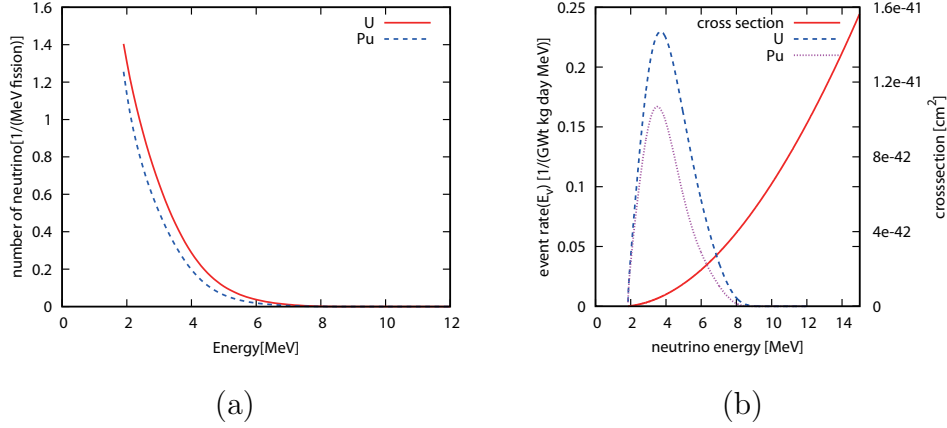


Figure 9: (a): The antineutrino spectra from ^{239}Pu and ^{235}U as emitted by a reactor. (b): Inverse beta decay cross section and detected antineutrino spectra which is the product of the emitted spectra and the cross section. It assumes that a 1-kg plastic scintillator detector at a standoff of 30 m from the reactor core.

tation property to reject the background events.

The plot on (a) in Fig. 9 shows the predicted energy spectra of antineutrinos per fission for the two most important fissile isotopes ^{239}Pu and ^{235}U [1]. The plot (b) shows the same spectra after folded with the energy-dependent cross section of the inverse beta decay. The folding is done by the equation:

$$N_{\bar{\nu},i}(E_{\bar{\nu}}) = \frac{TN_p}{4\pi D^2} \sigma(E_{\bar{\nu}}) \phi_i(E_{\bar{\nu}}). \quad (6)$$

In this equation, $N_{\bar{\nu},i}(E_{\bar{\nu}})$ is the number of antineutrino interactions per MeV in the detector in a time interval T from the i -th isotope. In practice the index runs over the four dominant fissioning isotopes ^{235}U , ^{238}U , ^{239}Pu and ^{241}Pu , which account for $\sim 99.9\%$ of fissions in a typical reactor. N_p is the number of target protons in the detector, D is the distance from the detector to the center of the reactor core. σ and ϕ_i are the cross section for the inverse

beta interaction and the antineutrino number density per MeV and second for the i -th isotope respectively. A cubic-meter-sized plastic scintillator detector at a standoff of 30 m from a reactor core is expected to measure $\sim 2.3 \times 10^3$ events per day, for 3 GWt power plant and a perfectly efficient detector.

We simulated positrons and neutrons produced via the inverse beta decay events uniformly distributed throughout the plastic scintillator volume, and recorded the total visible energy in each module. The energy and angular distributions of positrons and neutrons were derived from the inverse beta decay angular-differential cross section depending on the antineutrino energy $E_{\bar{\nu}}$ [10] and spectra shown in Fig. 9.

We used the Geant4 simulation toolkit[9] for simulating the passage of particles. To account for the optical photon response, we utilized the simple light propagation model described in Section 2. We simulated particle transport in the scintillators, the surrounding materials including the acrylic light guides, the PMTs, the aluminized Mylar films and the gadolinium coated Mylar films. Especially for the Lesser PANDA detector, the transport in the outer aluminum and wooden support structures were also simulated.

We modeled the resolution of the digitized signal $\sigma_{\text{sig}}(E)$ as

$$\sigma_{\text{sig}}(E) = \sqrt{\sigma_{\text{electronics}}^2 + \sigma_{\text{p.e.}}^2(E)}. \quad (7)$$

Here, the constant $\sigma_{\text{electronics}}$ represents the effect of the electric noise of the data acquisition system. It was determined by fitting the width of the pedestal distribution. $\sigma_{\text{p.e.}}(E) \equiv k\sqrt{E}$ is the variation in response caused by the finite number of photoelectrons generated in the event. Coefficient k for each module came out of the module calibration described in Section 3.

We applied the selection cuts shown in Table 2 to the simulation outputs

Table 2: The Antineutrino Event Selection Criterion

Prompt Energy	$3 \text{ MeV} \leq E_{\text{total}} \leq 10 \text{ MeV}$ $E_{1\text{st}} \leq 6 \text{ MeV}$ $200 \text{ keV} \leq E_{2\text{nd}} \leq 500 \text{ keV}$
Delayed Energy	$3 \text{ MeV} \leq E_{\text{total}} \leq 8 \text{ MeV}$ $E_{1\text{st}} \leq 5 \text{ MeV}$ $500 \text{ keV} < E_{2\text{nd}}$
Prompt-delayed interval	$6 \mu\text{s} < t_{\text{int}} < 200 \mu\text{s}$

Table 3: Detection Efficiency

	Lesser PANDA	PANDA
Target mass	160 kg	1000 kg
Detection efficiency	4.0%	11.6%
expected neutrino event rate (at 30m from a 3 GWt reactor)	15/day	$2.7 \times 10^2/\text{day}$

Table 4: Detection Efficiency of Each Stage of the Criteria

Quantity	Efficiency
Prompt	12%
Delayed	23%
time interval cut	89%
Total	4.0%

and estimated the detection efficiency. Prompt and delayed events were selected using the sum of the energy deposits of all the modules (E_{total}), the highest and the second highest values among all the modules ($E_{1\text{st}}, E_{2\text{nd}}$).

The threshold for the prompt total energy E_{total} was placed at 3 MeV so that all background gamma-rays were rejected here. The energy distribution of the antineutrino-generated positrons is directly related to the antineutrino energy distribution therefore no events with E_{total} beyond 10 MeV (6 MeV for $E_{1\text{st}}$) were admitted as extremely few antineutrino interactions were expected above these energies. The $E_{2\text{nd}}$ condition was set to tag the gamma rays created via annihilation of positrons.

The delayed total energy E_{total} threshold was also placed at 3 MeV. This threshold was set as high as possible to reject background gamma rays and low enough to retain as many delayed neutron events with cascading gamma rays from neutron capture by Gd as possible. Events with delayed energy of greater than 8 MeV were also excluded, as the predicted delayed energy was smaller than it. The $E_{2\text{nd}}$ threshold for delayed events was placed at 500 keV. Since more than one gamma rays with few MeV of energies are emitted from neutron capture by Gd, there are comparatively large number of events with $E_{2\text{nd}}$ greater than 500 keV. For the same reason, it is unlikely for the gamma rays to deposit such a large quantity of energy in one module. Therefore events with $E_{1\text{st}}$ greater than 5 MeV were discarded.

All values for the energy criteria were finally verified comparing energy spectra from the detector simulation and the background measurement. The detection efficiencies were comparatively insensitive to the energy cuts around these thresholds.

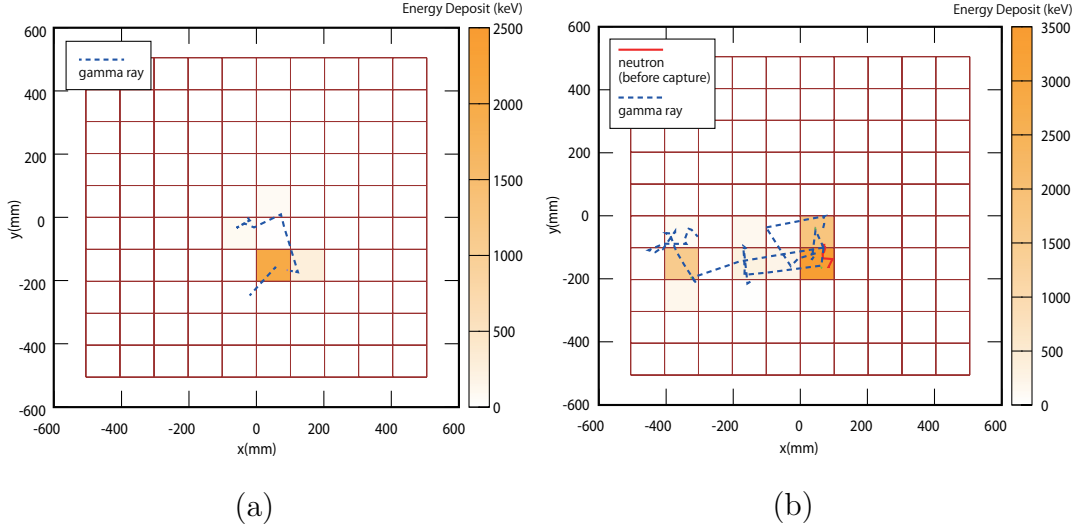


Figure 10: (a): Typical particle trajectories and energy deposit in the full size PANDA detector of a simulated antineutrino prompt event seen from the PMT side of the detector. (b): Corresponding delayed event.

The detection efficiency is also affected by the prompt-delayed interval cut. The interval distribution of antineutrino interactions is described by an exponential decay. According to the simulation result, the time constant of the exponential is about $60 \mu\text{s}$ and the interval cut of $200 \mu\text{s}$ means that only about 10% of the neutrino events are lost by this selection.

Table 3 shows the resulting total detection efficiencies and the expected event rates for the Lesser PANDA and the PANDA detectors. Table 4 shows the estimated efficiencies of each stage of our selection criteria.

Fig. 10 shows a typical simulated antineutrino event detected by the full size PANDA detector. A hit by a positron and one of two annihilation gamma rays are seen in the prompt event. Multiple hits of gamma rays emitted by Gd are also seen in the delayed event after $13 \mu\text{s}$ of the prompt event.

5. Background measurement

Ahead of the measurement at the commercial reactor, the Lesser PANDA detector was tested for two days in the van near the university building for background measurement. We counted the number of neutrino-like background events which are hardly distinguishable from the neutrino interaction and it amounted 981 ± 82 events/day.

The number of neutrino-like events were calculated as follows. First, we counted the number of events which satisfied all the selection criteria described in Table 2. Then we counted the number of accidental coincidences by applying the same criteria except for the prompt-delayed interval, which was changed to $1006\mu\text{s} < t_{\text{int}} < 1200\mu\text{s}$. The difference of these two numbers represents the number of events whose prompt and delayed signals had some correlation. We considered these correlated events as the neutrino-like backgrounds. The operation did not reduce the detection efficiency significantly. The subtraction of the accidental coincidence was important for our analysis because of fluctuating gamma-ray background especially during the measurement at the Hamaoka Nuclear Power Plant described below due to radioactive dust which originated in the Fukushima-1 nuclear power plant accident.

The detector was then deployed at Unit 3 of the Hamaoka Nuclear Power Plant of Chubu Electric Power Co., Inc. There are three operational reactors in this station; all of them are boiling water reactors and have maximum thermal (electric) power of 3.3–3.9GWt (1.1–1.4GWe) each. The detector was located by the reactor building of Unit 3 (3.3GWt) at a distance of 39.8 m from the reactor core. The Unit 3 reactor was under scheduled inspection

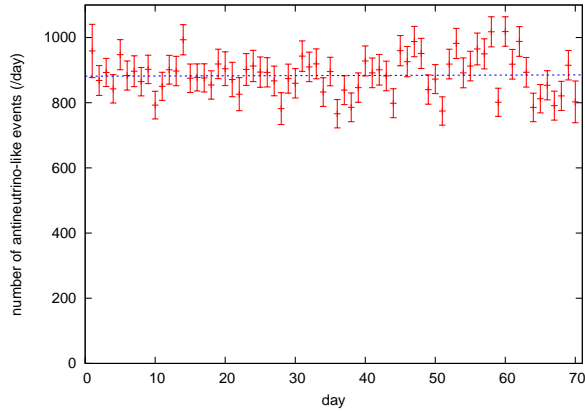


Figure 11: Daily number of correlated background events which satisfied the antineutrino selection criteria. Error bars are only statistical.

and was not in operation then ².

During a 70-day period of the background measurement, the average daily rate of neutrino-like events was distributed at 888 ± 70 events/day. The standard deviation is somewhat greater than the statistics due to as yet unknown reason. These events are comprised of non-antineutrino backgrounds. We observed no significant excess in the count rate compared to the rate measured near the university building.

A linear fit to the daily detection rate of antineutrino like events during reactor off period plotted versus day has a slope of 0.06 ± 0.36 events/day² (Fig. 11), which is consistent with a constant background.

The van with the detector on it was parking as close as possible to the

² We intended to measure the event rate change before and after a start up of the reactor when the inspection were over, but it did not start because of the general shutdown request by the Prime Minister after the Fukushima-1 nuclear power plant accident.

reactor building. There were no connections between the detector and the reactor building except a 100-volt AC power line, which supplied about 600 W of electricity for the whole detector system.

A hard disk drive with event data was replaced every two weeks and was carried back to Tokyo for the analysis. The detector system was otherwise operated without a human intervention throughout the period, and its status was monitored from the university in Tokyo via the cell phone network.

6. Discussion and conclusions

We proposed a new type of segmented antineutrino detector made of one hundred plastic scintillator bars wrapped in Gd-coated films for the nuclear safeguard application. The detector is all solid states and nonflammable. It is comparatively small, can be carried easily in a van and is intended to monitor a reactor from outside of the reactor building.

As a first step, a smaller prototype was built and tested near the university building and also near the reactor building of the nuclear power plant. The measured background rates were comparable on both the sites. We have shown that an unmanned operation is possible for a few months only with biweekly hard disk drive exchanges for the data collection.

A detailed Monte Carlo simulation code was developed for both the full size and prototype detectors. A detection efficiency of 11.6% and 4.0% were estimated for the full size and prototype detectors, respectively. Clearly, it would be hard to detect statistically significant number of antineutrino events with the prototype detector because of its low detection efficiency and relatively high measured background rate although current selection criteria

are not fully optimized yet.

With the full-size detector of effective target mass of 1 ton, we have a good chance to detect sufficient number of antineutrino events at reasonable standoff from commercial nuclear power stations.

7. Acknowledgements

The authors thank Chubu Electric Power Co.,Inc for its cooperation for our experiment on site of Hamaoka Nuclear Power Plant.

This research was partially supported by the Japanese Ministry of Education, Science, Sports and Culture, Grant-in-Aid for COE Research, Grant-in-Aid for Scientific Research (B), and Grant-in-Aid for JSPS Fellows and also by the Mitsubishi Foundation.

References

- [1] P. Vogel, J. Engel, *Phys. Rev. D* 39 (1989) 3378–3383.
- [2] T. A. Mueller, D. Lhuillier, M. Fallot, A. Letourneau, S. Cormon, M. Fechner, L. Giot, T. Lasserre, J. Martino, G. Mention, A. Porta, F. Yermia, *Phys. Rev. C* 83 (2011) 054615.
- [3] P. Huber, *Phys. Rev. C* 84 (2011) 024617.
- [4] Y. V. Klimov, V. I. Kopeikin, L. A. Mikaelyan, K. V. Ozerov, V. V. Sinev, *Atomic Energy* 76 (1994) 123–127.
- [5] A. Bernstein, Y. Wang, G. Gratta, T. West, *J. Appl. Phys.* 91 (2002) 4672.

- [6] A. Bernstein, N. S. Bowden, A. Misner, T. Palmer, J. Appl. Phys. 103 (2008) 074905.
- [7] N. S. Bowden, A. Bernstein, S. Dazeley, R. Svoboda, A. Misner, T. Palmer, J. Appl. Phys. 105 (2009) 064902.
- [8] H. Furuta, et al., Nucl. Instrum. Meth. A 662 (2011) 90–100.
- [9] S. Agostinelli, et al., Nucl. Instrum. Meth. A 506 (2003) 250–303.
- [10] P. Vogel, J. F. Beacom, Phys. Rev. D 60 (1999) 053003.